metals

Article

Research on Microstructural Characterization and Mechanical Properties of Al-Zn-Mg-Cu Alloy Thick Plate During Rolling

Guiying Deng [1,2,†], Yaohui Wang [3,†], Xu Zheng [2,*], Xinkui Zhang [1], Kai Ma [3,*], Bolu Xiao [3] and Zongyi Ma [3]

[1] National Engineering Research Center of Near-Net Shape Forming Technology for Metallic Materials, South China University of Technology, Guangzhou 510640, China; vita_deng@163.com (G.D.); xinkuizhang1996@163.com (X.Z.)
[2] Guangxi Nannan Aluminum Processing Co., Ltd., Guangxi Key Laboratory of Aluminum Alloy Materials and Processing, Nanning 530031, China
[3] Institute of Metal Research, Chinese Academy of Sciences, Shenyang 110016, China; 17717164822@163.com (Y.W.); blxiao@imr.ac.cn (B.X.); zyma@imr.ac.cn (Z.M.)
* Correspondence: zhengxu_gig@163.com (X.Z.); kma16s@imr.ac.cn (K.M.)
† These authors contributed equally to this work.

Abstract

This study investigated how initial ingot thickness (400 mm vs. 520 mm) influences the microstructure and mechanical properties of Al–Zn–Mg–Cu alloys rolled to 80 mm. The combination of smaller initial thickness and lower total reduction (the 400-L route) results in lower dislocation density and a higher fraction of metastable η′ precipitates after T77 treatment. In contrast, the 520-L route, which involves a larger initial ingot thickness coupled with greater rolling reduction, yields higher dislocation density and a greater proportion of stable η phase. Texture also differs: the 400 mm ingot develops a strong S texture and high anisotropy, whereas the 520 mm ingot exhibits Brass texture and reduced anisotropy. Specifically, cross-rolling plus longitudinal rolling of the 520 mm ingot enhances recrystallization texture, giving a short-transverse yield strength of 528 MPa—within 6% of the longitudinal direction. This work offers valuable insights for controlling anisotropy in large 7xxx aluminum plates.

Keywords: 7xxx-series aluminum alloy; large-scale ingots; rolling processes; texture; anisotropy; T77 temper

1. Introduction

The 7xxx-series aluminum alloys, primarily alloyed with Al-Zn-Mg-Cu, have emerged as critical strategic materials in the aerospace sector due to their high specific strength, excellent fatigue resistance, and other advantageous properties. They are widely employed in core load-bearing components such as aircraft skins and door protection structures [1–3]. With rising application demands, research on forming processes for these high-strength aluminum alloys has garnered increasing interest. In addition to conventional rolling and extrusion processes, unconventional forming methods such as the KOBO extrusion technique have also been explored for processing these high-strength alloys, demonstrating the potential for achieving refined microstructures and enhanced mechanical properties under complex strain paths [4]. With the increasing integration of aerospace equipment, there is a surging demand for large-scale, integrated high-performance plate components. This drives a paradigm shift in the production of 7xxx-series aluminum alloy plates—from the conventional approach of "small-to-medium-sized ingots with subsequent

Check for updates

Academic Editor: Zbigniew Pater

Received: 5 March 2026
Revised: 20 April 2026
Accepted: 23 April 2026
Published: 14 May 2026

Copyright: © 2026 by the authors. Licensee MDPI, Basel, Switzerland. This article is an open access article distributed under the terms and conditions of the Creative Commons Attribution (CC BY) license.

rolling" to that of "large-sized ingots with heavy-reduction rolling". Compared to conventional smaller ingots, producing plate components of the same thickness specification using large-scale ingots necessitates increased rolling deformation. This enhanced deformation helps eliminate casting defects like porosity and shrinkage, while simultaneously reducing the number of melting cycles, saving energy, and increasing production efficiency. This approach aligns with the core objectives of modern manufacturing: cost reduction and efficiency improvement [5–9].

However, the rolling of large-scale ingots presents several challenges: The slow cooling rates during solidification promote the formation of coarse grains, which significantly degrade mechanical properties [10–12]. Multi-pass rolling can refine the microstructure to some extent; however, severe plastic deformation elongates and fragments grains, leading to the formation of directional fibrous structures. This, in turn, induces significant anisotropy in the plate properties [13–16]. For instance, Wei et al. [17] investigated the static tensile properties of a 7050 aluminum alloy plate and observed pronounced strength anisotropy. The yield strength was highest in the longitudinal (L) direction and lowest in the short-transverse (ST) direction, with a difference exceeding 10% between the two. Such anisotropy not only complicates consistent quality control but also poses potential risks to the reliability of components in service.

Recent studies have shown that cross-rolling—where the rolling direction is altered between passes, effectively reorienting the previously widened direction to become the new elongation direction—can effectively mitigate anisotropy [18–20]. For example, in a study on rolling 20 mm thick 2xxx-series aluminum alloy plates, Sun Dongpeng et al. [21] found that plates produced by cross-rolling exhibited a 58.93% reduction in the difference between transverse and longitudinal tensile strength and a 15.56% decrease in the anisotropy of elongation compared to those produced by conventional unidirectional rolling, significantly reducing planar anisotropy. Similarly, Amir Kazemi Navaee et al. [22], investigating the single-roll-driven cross-rolling behavior of 6 mm thick AA7075 aluminum alloy, reported a substantial decrease in planar anisotropy with increasing rolling reduction. However, these studies focused exclusively on cross-rolling of aluminum alloy sheets with thicknesses below 20 mm. The effectiveness of this technique for controlling anisotropy in thick aluminum alloy plates remains insufficiently explored. Compared to sheet rolling, the deformation zone in thick plates is more complex, and regions far from the rolled surface often experience insufficient deformation [23], which may compromise the effectiveness of cross-rolling in regulating anisotropic microstructures. Therefore, investigating the influence of cross-rolling on the microstructural and property evolution of thick 7xxx-series aluminum alloy plates is crucial for enhancing the quality of their industrial production.

The heat treatment employed in this study is the T77 temper, a specialized three-stage aging treatment developed specifically for 7xxx-series aluminum alloy thick plates. The T77 temper produces a characteristic microstructure consisting of fine intragranular metastable η' precipitates, together with coarse, discrete grain-boundary η particles and distinct precipitate-free zones. This microstructural configuration enables the alloy to retain near-peak strength (comparable to the T6 temper) while exhibiting substantially enhanced resistance to both stress corrosion cracking (SCC) and exfoliation corrosion—a property profile that is critically required for thick-plate applications in primary load-bearing aerospace structures such as upper wing skins and fuselage frames. Given that the precipitation response during T77 aging is highly sensitive to the crystal defects introduced during prior deformation, the rolling history—particularly the total reduction and the rolling path—can markedly influence the resultant precipitate characteristics. Elucidating how different rolling strategies modulate the microstructure and mechanical properties

of T77-treated thick plates is therefore of both fundamental scientific interest and direct practical relevance to industrial manufacturing.

This study systematically investigates the rolling processing of two typical ingot thicknesses: 400 mm and 520 mm. In contrast to prior investigations focused on the cross-rolling of thin sheets, the present study targets the characteristic insufficient deformation in the core region of thick plates. It demonstrates that the cross-rolling-induced transformation of the dominant texture component from S {123}<634> to Brass {011}<211>, rather than a simple randomization of texture intensity, is the critical mechanism governing the reduction in short-transverse mechanical anisotropy in thick 7xxx aluminum plates. Furthermore, crystallographic calculations were employed to quantitatively elucidate the strengthening mechanism by which the Brass texture enhances the short-transverse mechanical properties. A multi-scale "processing–texture–precipitation–property" correlative framework was established for industrial-scale thick plates, thereby providing both a mechanistic rationale and actionable processing guidelines for anisotropy control in load-bearing aerospace structural components.

2. Methods

The ingots were produced using molds of two thicknesses: 440 mm and 550 mm. The actual chemical composition is given in Table 1. For subsequent rolling processes, the 440 mm thick ingot was machined into a 400 × 1820 mm slab prior to rolling, while the 550 mm thick ingot was machined into a 520 × 2530 mm slab. Rolling was performed with temperature strictly maintained at 420 °C and speed stabilized at 1.5 m/s to ensure experimental consistency and controllability. The reduction per pass was controlled at approximately 15%, resulting in a final plate thickness of 80 mm. Calculated deformation ratios reached 80% for the 400 × 1820 mm slab and 85% for the 520 × 2530 mm slab. For the 520 × 2530 mm slab, two distinct rolling strategies were implemented. The first strategy employed unidirectional rolling, where deformation proceeded exclusively along a single fixed direction through multiple passes. The second method involved rotating the plate by 90° when its thickness approached ~450 mm, followed by longitudinal rolling along the original width direction to achieve controlled width spreading. This cross-rolling strategy aimed to modify material deformation paths and microstructural evolution through directional changes. Samples were systematically labeled for identification: 400-L (unidirectional rolling of 400 × 1820 mm slab), 520-L (unidirectional rolling of 520 × 2530 mm slab), and 520-LT (520 × 2530 mm slab with width spreading + longitudinal rolling). The material orientations are defined as follows (Figure 1): L-direction (final rolling direction), LT-direction (transverse direction), and ST-direction (short-transverse direction). The rolled samples underwent a solution heat treatment at 470 °C for 120 min followed by 482 °C for 120 min, with subsequent water quenching. They were then subjected to a T77 aging treatment: 120 °C for 24 h + 160 °C for 5 h, followed by water quenching and a final aging step at 120 °C for 24 h.

Table 1. Chemical composition of the Al-Zn-Mg-Cu alloy (wt.%).

Si	Fe	Cu	Mg	Zn	Ti	Zr	Al
0.03	0.04	2.18	1.68	8.20	0.025	0.10	Bal.

Microstructural analysis was conducted using a Leica DMi8 M optical microscope (OM), Zeiss Gemini Sigma 500 scanning electron microscope (SEM), and FEI Talos F200X transmission electron microscope (TEM), complemented by electron backscatter diffraction (EBSD). Metallographic specimens were ground, polished, and etched with Keller's reagent,

while EBSD specimens were prepared by grinding followed by electrolytic polishing with a solution of 10%$HClO_4$ + 90%C_2H_6O. Geometrically necessary dislocation (GND) density maps were calculated from the EBSD data using AZtecCrystal software (version 2.1). The calculation is based on the Nye–Kröner framework, in which the lattice curvature tensor is derived from the orientation gradients between adjacent measurement points. The orientation gradient is determined from misorientations represented in quaternion form, and the curvature tensor is obtained via least-squares fitting. The lower-bound GND density is subsequently estimated from the Nye tensor using an L1-norm minimization algorithm. A step size of 3 μm was employed during EBSD data acquisition. Pixels with a confidence index (CI) below 0.1 were excluded from the analysis to minimize noise-induced artifacts. The GND density values reported in this work represent the arithmetic mean over all valid pixels within the respective scanned areas. For TEM characterization, the discs with a diameter of 3 mm were ground to a thickness of 90 μm and electrochemically polished using a twin-jet electron-polishing device with a solution of 30%HNO_3 + 70%CH_3OH at −25 °C.

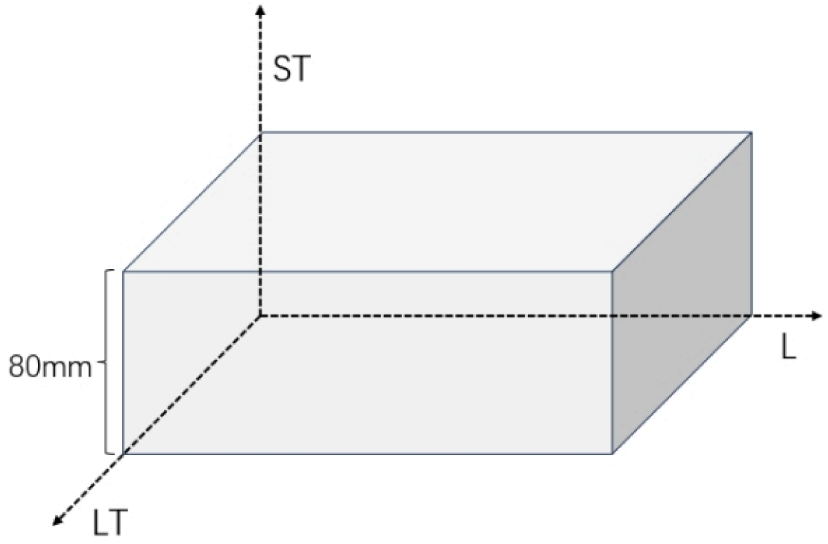


Figure 1. Schematic illustration of orientation calibration for the rolled plate.

To evaluate rolling-process effects on mechanical properties, tensile bars with a gauge diameter of 10 mm were extracted from the quarter-thickness location of plates produced by all three processes. The tensile tests were performed using a WANCE TSE504D universal testing machine at a strain rate of 1×10^{-3} s^{-1}.

3. Results

3.1. Microstructure

Figure 2 presents OM images of samples parallel to the rolling plane under the three rolling processes. The results reveal that all samples exhibit distinct mixed-grain structures, characterized by the coexistence of grains with significantly different sizes. Further comparison demonstrates that the width of coarse grain bands in the 400-L sample is slightly reduced compared to those in the 520-L and 520-LT samples. This phenomenon can be primarily ascribed to the smaller mold size employed for the 400-L ingot, which promoted faster cooling and consequently a finer as-cast grain structure. It should be noted, however, that the 520-L and 520-LT specimens also underwent a greater total rolling reduction, which contributed to the observed differences in grain morphology.

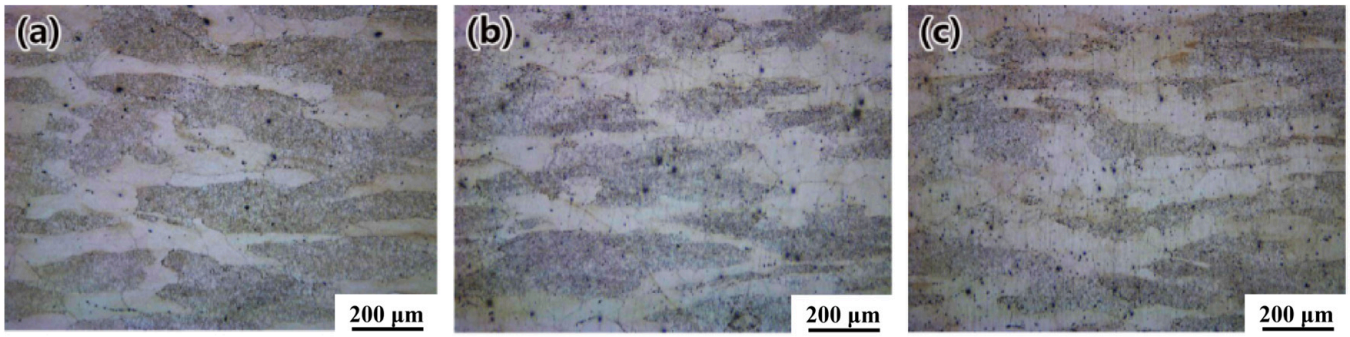


Figure 2. Observation results along the rolling plane direction (observation plane perpendicular to the ST direction): (**a**) 400-L, (**b**) 520-L, (**c**) 520-LT.

When observed along the rolling side plane (the plane defined by the rolling direction and normal direction of the plate), the banded structural feature becomes more pronounced, as shown in Figure 3. Compared to the rolling plane, these banded structures appear significantly finer. Notably, this observation reveals a contrasting trend to that of the rolling plane: the coarse grain band width in the 400-L sample is slightly larger than that in the 520-L and 520-LT samples. This may be attributed to the greater thickness reduction experienced by the 520-L and 520-LT ingots during rolling. The enhanced thinning effect along the longitudinal direction reduced the coarse grain bands more substantially, resulting in narrower band widths on the rolling side plane.

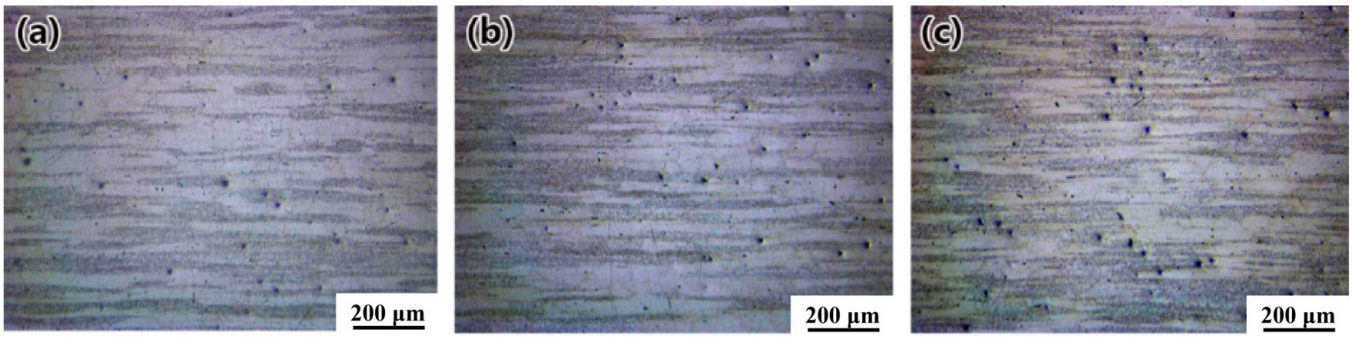


Figure 3. Observation results along the rolling side direction (observation plane perpendicular to the LT direction): (**a**) 400-L, (**b**) 520-L, (**c**) 520-LT.

EBSD characterization was further conducted to investigate the microstructures of the specimens prepared under the three kinds of rolling processes, with results presented in Figure 4. Figure 4a–c show the inverse pole figure (IPF) maps along the rolling plane direction, revealing average grain sizes of 29.1 μm, 30.2 μm, and 29.7 μm for the 400-L, 520-L, and 520-LT samples, respectively. Figure 4d–f present the IPF maps along the rolling side plane, with corresponding grain sizes of 22.8 μm, 25.9 μm, and 24.8 μm. Comparative analysis demonstrates that regardless of observation direction (rolling plane or side plane), the grain sizes of the 520-L and 520-LT samples are slightly larger than that of the 400-L sample, in agreement with the change in coarse grain band widths previously observed via OM. Consistent with earlier studies, the 400-L ingot was prepared using a smaller mold, yielding finer initial grains. Although the 520-L and 520-LT ingots underwent greater deformation during rolling, their larger initial ingot dimensions and solidification conditions likely contributed to their relatively coarser final grain sizes.

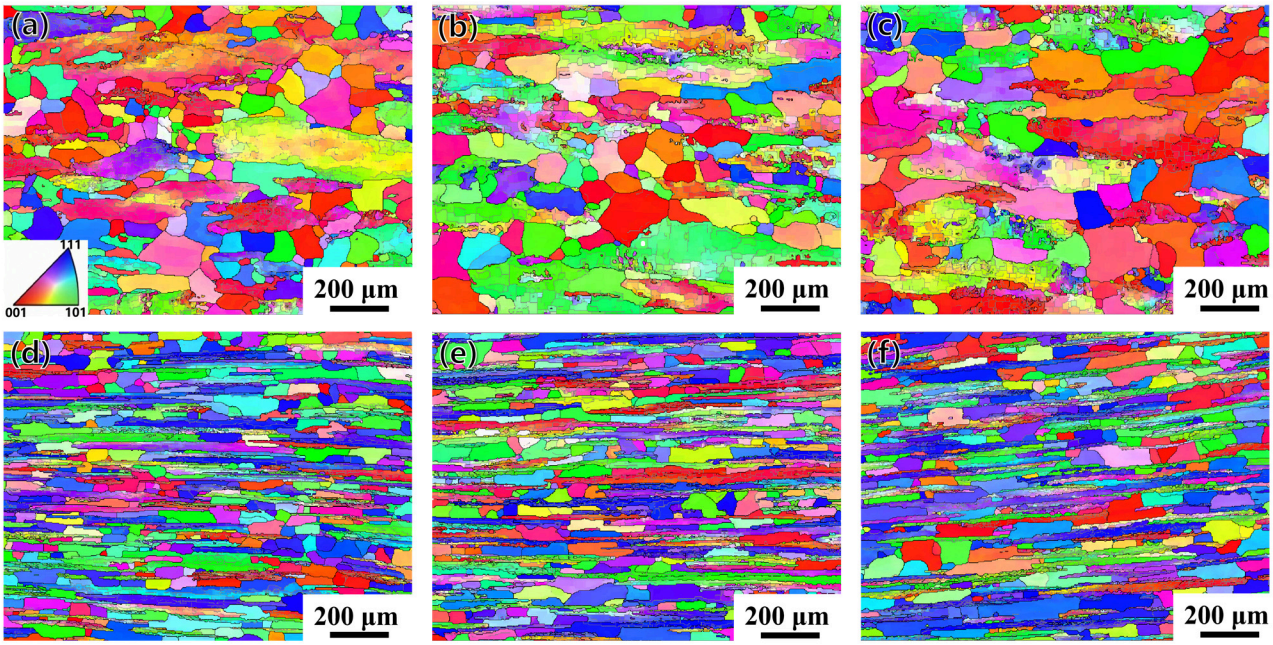


Figure 4. EBSD inverse pole figure (IPF) maps: (**a**,**d**) 400-L; (**b**,**e**) 520-L; (**c**,**f**) 520-LT. (**a**–**c**) Rolling plane; (**d**–**f**) rolling side plane.

Figure 5 displays the geometrically necessary dislocation (GND) density distribution maps of materials processed via the three rolling techniques: 400-L, 520-L, and 520-LT. Visually, regions of high GND density are predominantly concentrated within fragmented grain structures. During rolling deformation, these finely fragmented grains experienced complex stress states and deformation heterogeneity, promoting substantial dislocation accumulation and consequently forming high-GND-density zones. Quantitative analysis reveals GND densities of 3.5×10^{13} m^{-2}, 1.52×10^{14} m^{-2}, and 1.52×10^{14} m^{-2} for the 400-L, 520-L, and 520-LT samples, respectively. Both 520-L and 520-LT exhibit significantly higher GND densities compared to 400-L. This phenomenon correlates directly with their distinct deformation processes. The 520-L and 520-LT ingots underwent greater thickness reduction during rolling. This severe deformation induced pronounced alterations in the crystalline structure, driving extensive dislocation multiplication and mutual entanglement, thereby substantially elevating GND density. Conversely, the 400-L sample, processed from a smaller initial ingot, experienced relatively lower overall deformation. This constrained dislocation multiplication resulted in comparatively lower GND density.

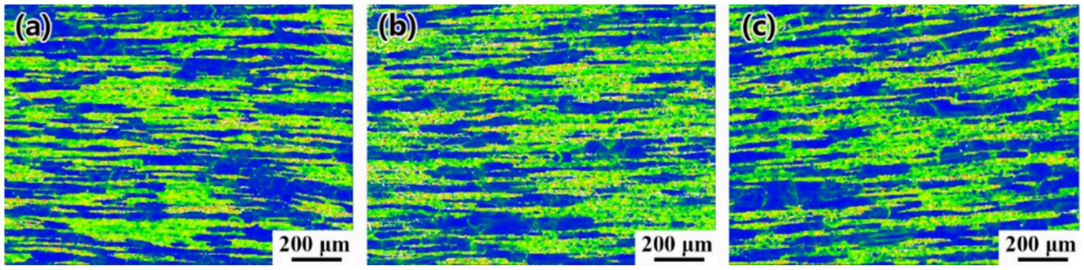


Figure 5. GND density distribution maps: (**a**) 400-L, (**b**) 520-L, (**c**) 520-LT. The GND density values represent the arithmetic mean over all valid pixels within the respective scanned areas.

3.2. Texture Analysis

To characterize texture evolution under different rolling processes, orientation distribution function (ODF) maps at $\varphi 2 = 0°$, 45°, 65° sections were comprehensively constructed and are presented in Figure 6. Figure 6a identifies standard texture components using

color-coded markers within the 2D ODF space, encompassing typical texture types observed during rolling: rolling textures including Goss {011}<100>, S {123}<634>, Brass {011}<211>, Dillamore {4 4 11}<11 11 8>, and Copper {112}<111>; and shear textures such as E {111}<110>, Rotated Cube {001}<110>, Inverse Brass {112}<110>, and F {111}<112>; along with the recrystallization texture Cube {001}<100>. During aluminum alloy sheet processing, the formation and evolution of these distinct textures vary significantly with rolling parameters, thereby exerting marked effects on material properties. Figure 6b–d present ODF maps at φ_2 = 0°, 45°, and 65° for the 400-L, 520-L, and 520-LT samples, where significant differences in both texture components and intensity were observed.

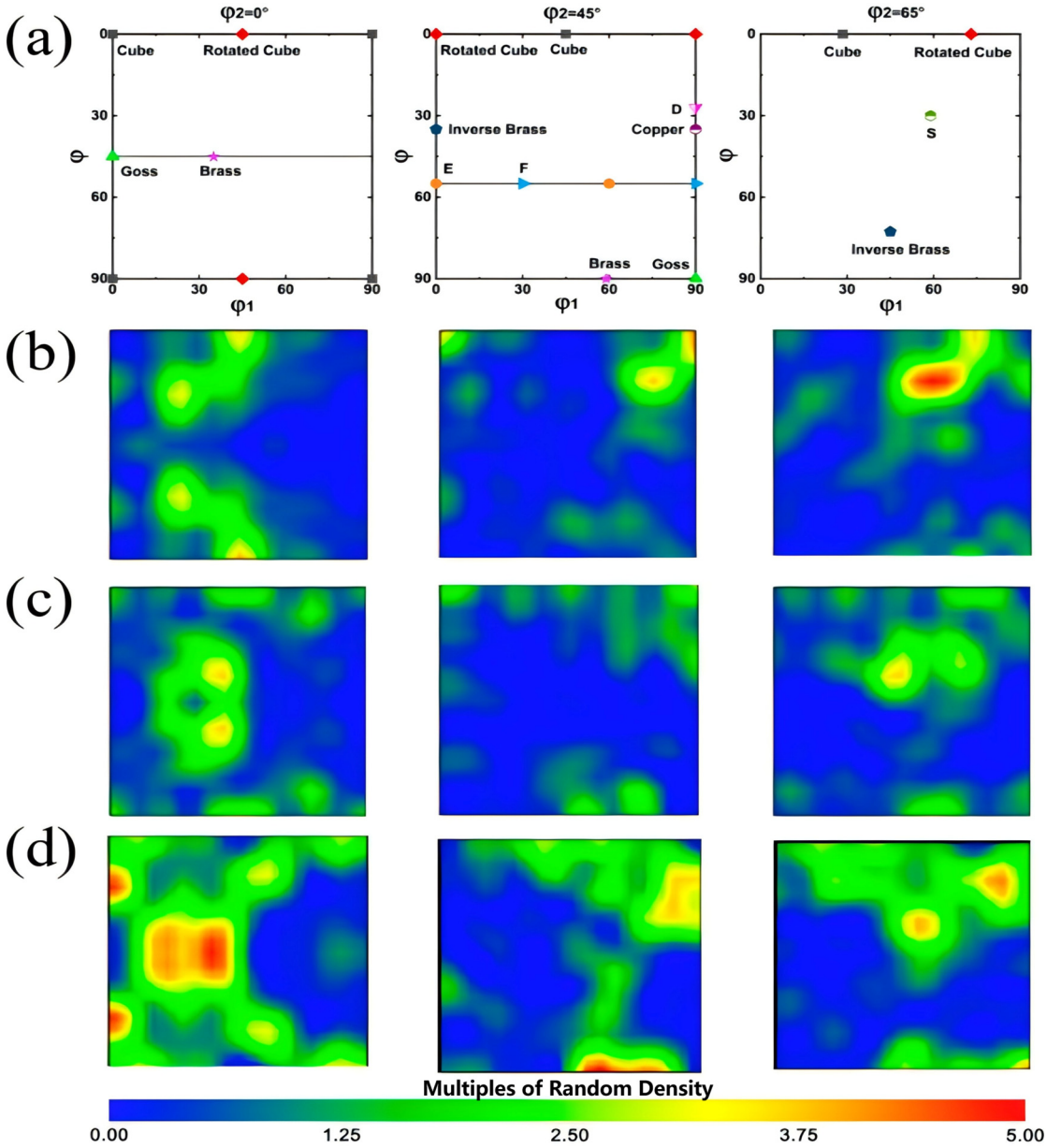


Figure 6. (**a**) Schematic illustration of ideal texture positions on φ_2 = 0°, 45°, and 65° sections, and ODF maps of (**b**) 400-L, (**c**) 520-L, and (**d**) 520-LT specimens.

To elucidate the influence of different processing routes on texture components in aluminum alloy sheets, the volume fractions of texture constituents were systematically quantified (Figure 7). All processed sheets exhibit pronounced rolling texture characteristics, indicating that directional material flow induced by rolling dominates texture

formation. Specifically, the 400-L processed sheet shows S {123}<634> as its dominant texture component, whereas Brass {011}<211> constitutes the primary texture in both 520-L and 520-LT processed sheets. This divergence in dominant texture types reflects the combined influence of initial ingot dimensions and the total rolling reduction on the evolution of crystallographic orientation.

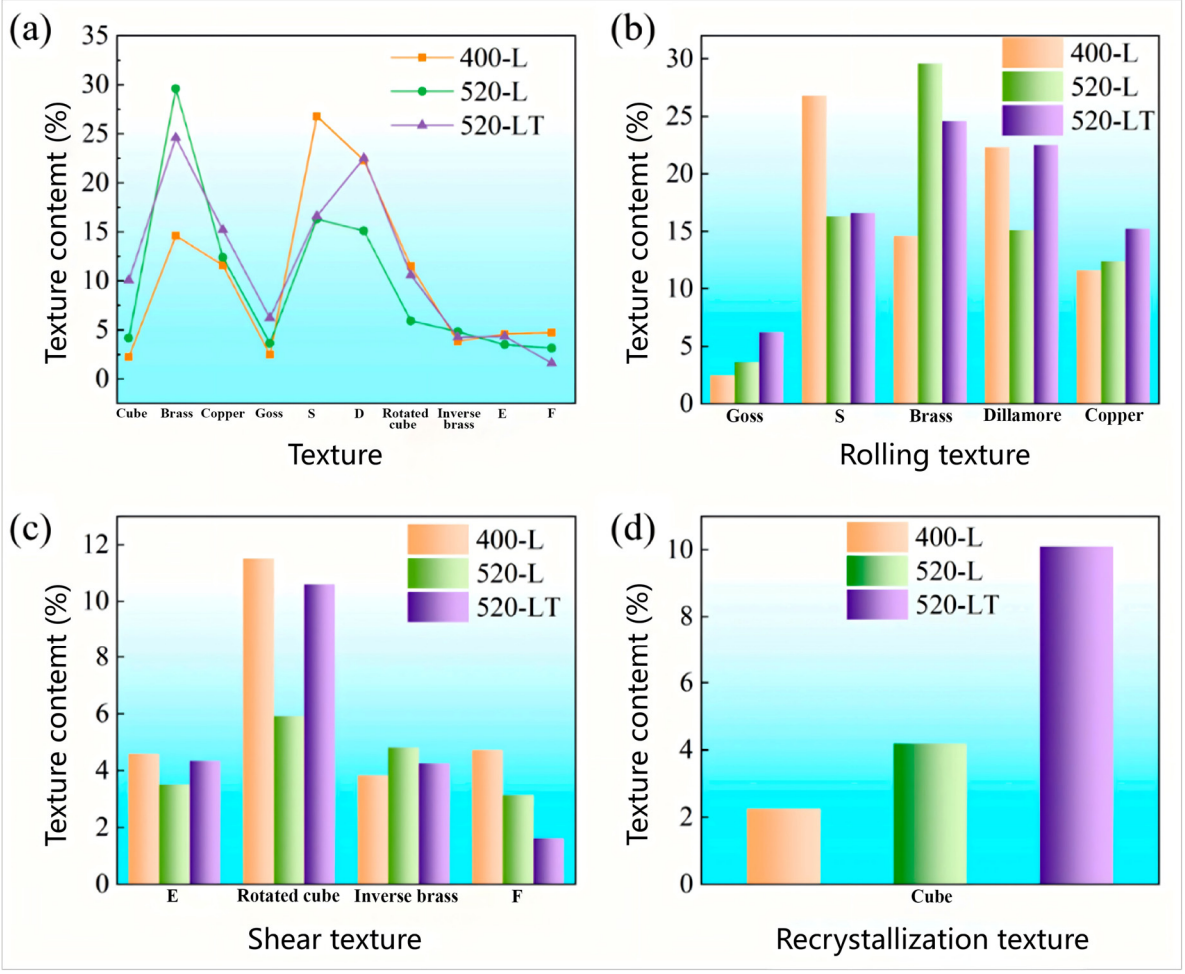


Figure 7. Statistical analysis of texture components in plates processed by the three rolling routes: (**a**) all textures, (**b**) rolling textures, (**c**) shear textures, and (**d**) recrystallization textures.

Regarding shear texture content, the 520-L and 520-LT sheets exhibit significantly higher fractions of E, Rotated Cube, and F shear textures compared to the 400-L sheet, which is attributed to the greater number of rolling passes experienced by the 520 mm thick ingots. As deformation progressed, directional material flow became progressively enhanced, thereby suppressing shear effects during crystal deformation and ultimately reducing shear texture formation.

Regarding recrystallization texture content, the 400-L, 520-L, and 520-LT sheets exhibit a progressively increasing trend, with the 520-LT sheet demonstrating the highest fraction. This result may be attributed to two factors: Firstly, the substantial deformation strain accumulated in the 520-LT sheet during rolling provides enhanced driving force for recrystallization, promoting more extensive grain restructuring. Secondly, its bidirectional rolling deformation simultaneously induces recrystallization of preferentially oriented grains along both orthogonal directions, further amplifying recrystallization texture development.

3.3. Precipitate Morphology

Figure 8 shows the microstructures of the three materials under different rolling processes after T77 heat treatment. All three materials exhibit distinct precipitate-free zones (PFZs) along grain boundaries. The PFZ widths for the 400-L, 520-L, and 520-LT conditions were approximately 45 nm, 48 nm, and 47 nm, respectively, indicating comparable extents. Further observation of the intragranular precipitates reveals a mixture of rod-like and spherical morphologies in all cases. Based on the high-resolution TEM (HRTEM) characterization of the 520-L condition (Figure 8g,h), the rod-shaped precipitates are identified as metastable η′ phase, maintaining an Al[-100] // η′[2-1-10] orientation relationship with the matrix. The spherical precipitates are the stable η phase, with an Al[-100] // η[10-10] orientation relationship with the matrix. The relative proportions of the η′ and η phases vary with the rolling process. The 400-L condition contains a higher fraction of fine η′ precipitates, whereas the 520-L and 520-LT conditions show a reduced proportion of η′ phase and a higher content of coarser η phase. This indicates that, despite the identical heat treatment, variations in the rolling process lead to corresponding changes in the morphology of the precipitates.

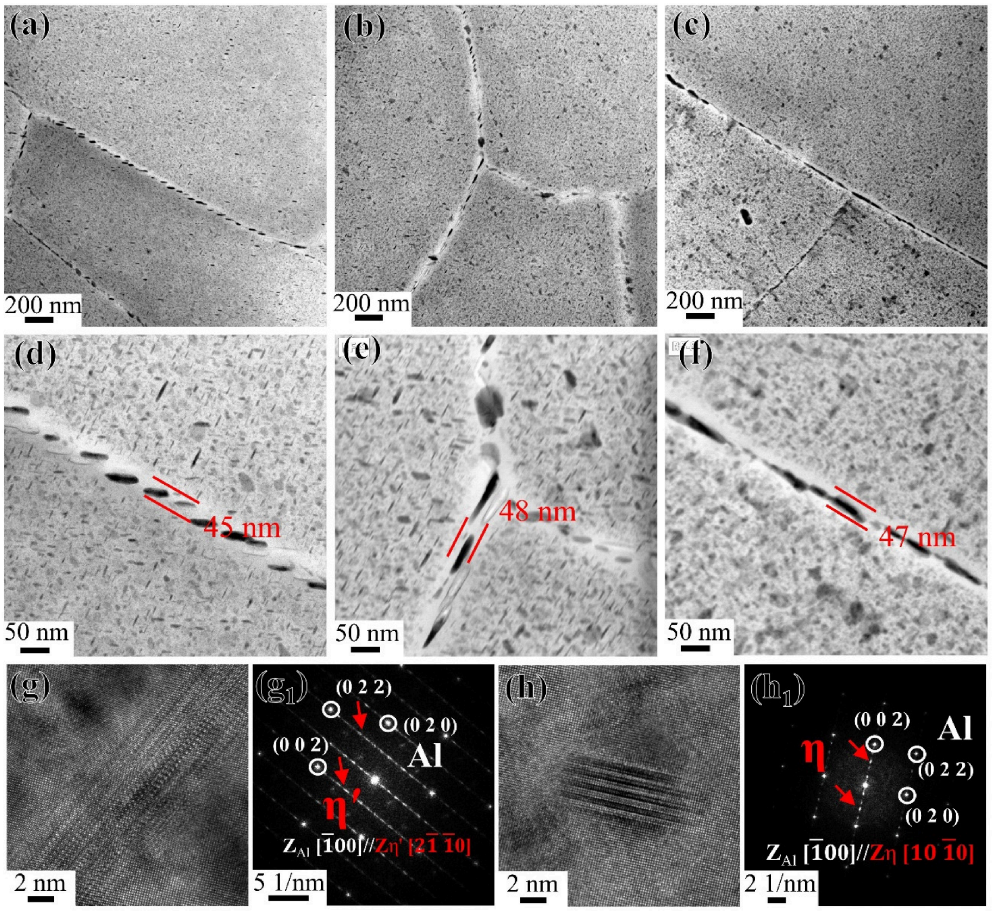


Figure 8. Morphologies of precipitates under three rolling routes: BF-TEM images of (**a**,**d**) 400-L; (**b**,**e**) 520-L; and (**c**,**f**) 520-LT samples; and (**g**,**h**) HRTEM and (**g1**,**h1**) corresponding FFT images of 520-LT.

For 7xxx-series aluminum alloys, the typical aging precipitation sequence is: super-saturated solid solution (SSS) → Zn-, Mg- (Cu-) rich clusters or coherent GP zones → metastable η′ phase → stable η phase [24]. Previous studies have shown that an increased dislocation density accelerates the nucleation and growth of precipitates [25,26]. Combined with the dislocation density statistics in Figure 5, the 520-L and 520-LT samples, which

underwent greater rolling deformation, exhibit a significantly higher dislocation density than the 400-L sample. This promotes the transformation of the metastable η′ phase into the stable η phase, resulting in a lower fraction of η′ phase and a higher content of η phase in the 520-L and 520-LT conditions. Notably, the number density of aging precipitates within the grains of the 520-L sample is lower than that in the 520-LT sample. This difference is likely attributable to the cross-rolling deformation used for the 520-LT sample. This deformation mode introduces more dislocations and vacancies during hot deformation, providing a greater number of nucleation sites in the early stages of artificial aging. Consequently, the 520-LT condition ultimately achieves a higher precipitate number density compared to the 520-L condition.

3.4. Tensile Properties

To comprehensively investigate the effect of different rolling processes on the mechanical properties of aluminum alloy thick plates, tensile specimens were extracted from the quarter-thickness (T/4) location and tested along the L, LT, and ST directions. For each processing condition and test direction, three parallel specimens were evaluated to ensure statistical reliability. As shown in Figure 9, the 400-L sample exhibits significant mechanical anisotropy. Its yield strength and elongation are comparable in the L and LT directions but substantially higher than those in the ST direction. This mechanical anisotropy may arise from elemental segregation between layers during rolling, leading to insufficient interlayer bonding strength and consequently diminished strength–ductility in the ST direction [27–29], consistent with typical rolled materials. The 520-L sample demonstrates distinct mechanical behavior. While its L-direction yield strength exceeds that in the LT direction, it is slightly lower compared to the 400-L sample. Conversely, the ST-direction yield strength of 520-L surpasses that of 400-L. Regarding the 520-LT material, its L- and LT-direction properties are similar to 520-L, but ST-direction strength shows significant enhancement. Further analysis indicates that the reduced strength of the 520-L and 520-LT samples in certain directions primarily correlates with their larger grain sizes. The diminished fine-grain strengthening effect in these samples contributes to strength reduction. The relative strength variations between the LT and ST directions require in-depth analysis considering texture evolution.

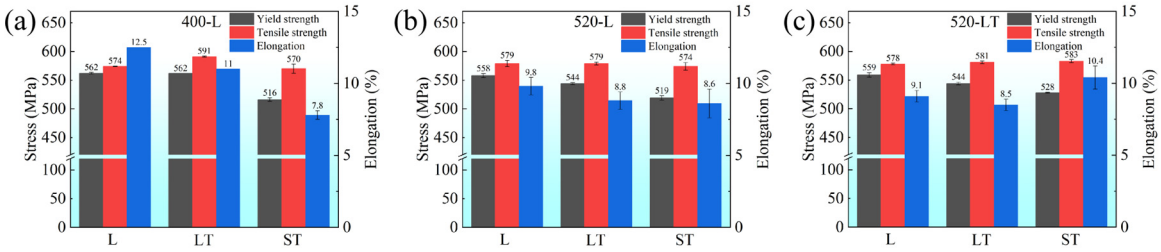


Figure 9. Tensile properties of plates processed by different rolling routes: (**a**) 400-L, (**b**) 520-L, (**c**) 520-LT.

3.5. Anisotropy Analysis

It is well established that the strength of heat-treatable aluminum alloys exhibits critical dependence on the morphology of age-hardening precipitates [30–33]. The strength anisotropy of heat-treatable Al-Zn-Mg-Cu alloys is closely associated with precipitate distribution on {111} habit planes, where $MgZn_2$ phases preferentially form. These precipitates act as nanoscale obstacles that impede dislocation motion, providing higher resistance to deformation when the loading direction aligns with the {111} planes. Under external loading, different crystallographic planes experience distinct stress states. The unique

precipitate distribution along {111} habit planes plays a crucial role in resisting deformation, as schematically shown in Figure 10.

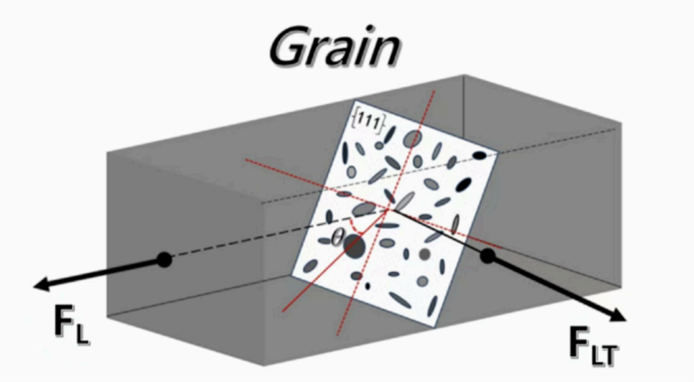


Figure 10. Schematic illustration of the stress state on the MgZn2 habit plane under external loading.

Based on the equation of the load transfer effect [34]:

$$F_\theta = \left\{ \frac{\cos^4\theta}{{F_L}^2} + \left(\frac{1}{{F_{LT}}^2} - \frac{1}{{F_L}^2} \right) \cos^2\theta \sin^2\theta + \frac{\sin^4\theta}{{F_{ST}}^2} \right\}^{-\frac{1}{2}} \quad (1)$$

where F_L, F_{LT}, and F_{ST} denote the strength components along the three principal directions of the strengthening interface, with θ representing the angle between the loading direction and strengthening interface. This relationship indicates that smaller θ values correspond to higher load-bearing capacity F_θ of the strengthening interface, thereby enhancing material strength.

To elucidate the fundamental mechanisms governing mechanical property differences in aluminum alloy plates processed via distinct rolling routes (400-L, 520-L, and 520-LT), systematic analysis was conducted from the perspective of dominant texture components. Quantitative texture statistics in Figure 7 reveal S {123}<634> as the predominant texture in 400-L plates, while Brass {011}<211> dominates both 520-L and 520-LT plates. These divergent texture types directly influence crystallographic orientation distributions, critically determining directional mechanical properties.

Figure 11 schematically illustrates orientation characteristics of Brass and S textures relative to plate directions. Calculated angles between loading directions (L/LT) and habit planes (Table 2) show that for S-texture-dominated 400-L plates, the minimum angles are 4.24° (L), 4.53° (LT), and 0° (ST). According to Equation (1), smaller angles enhance strengthening effects from high-density precipitates (e.g., $MgZn_2$ phases in Al-Zn-Mg-Cu alloys) on habit planes. Consequently, the comparable L and LT angles (4.24° vs. 4.53°) yield similar strengthening effects, explaining the nearly identical L/LT strength in 400-L.

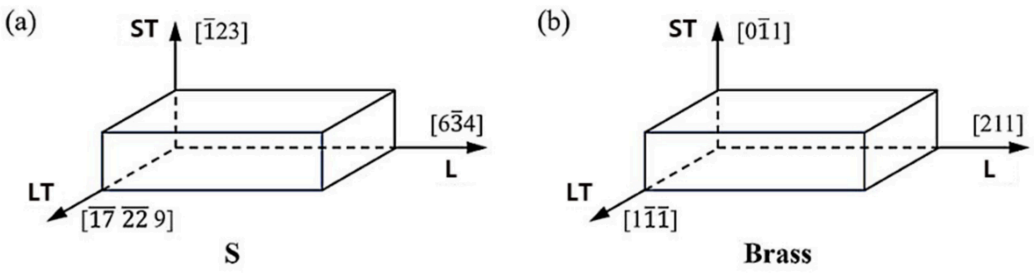


Figure 11. Schematic illustration of the crystallographic orientations of different texture types in the rolled plates: (**a**) S texture and (**b**) Brass texture.

Table 2. Angles between the Brass/S textures and the habit plane.

Texture	Habit Plane	Loading–Habit Plane Angle		
		L	LT	ST
Brass	{111}	70.53°	19.47°	0°
	$\{\bar{1}11\}$	0°	90°	0°
	$\{1\bar{1}1\}$	28.12°	19.47°	54.74°
	$\{11\bar{1}\}$	28.12°	19.47°	54.74°
S	{111}	31.17°	36.35°	38.11°
	$\{\bar{1}11\}$	21.69°	4.53°	67.79°
	$\{1\bar{1}1\}$	73.94°	16.06°	0°
	$\{11\bar{1}\}$	4.24°	71.50°	17.97°

For Brass-texture-dominated plates (520-L/520-LT), the minimum angles measure 0° (L), 19.47° (LT), and 0° (ST). The parallel alignment (0°) between L-direction loading and habit planes maximizes precipitate strengthening, while the substantial LT angle (19.47°) weakens strengthening. This directly accounts for lower LT-direction yield strength in 520-L/520-LT samples. Notably, although both textures exhibit 0° ST-direction angles, their strengthening efficiencies differ fundamentally. Brass texture achieves 0° angles on two habit planes ({111} and {−111}), whereas S texture attains this only on {1−11}. Consequently, Brass texture activates more strengthening interfaces along ST, yielding higher efficiency that mitigates normal-direction (ST) strength attenuation. This explains the significantly enhanced ST-direction strength in 520-L/520-LT plates versus 400-L. Further comparison demonstrates superior ST-direction strength in 520-LT relative to 520-L, with significantly reduced anisotropy between the ST direction and the in-plane (L and LT) directions. This mechanical property homogenization indicates mitigated anisotropy in 520-LT, attributable to its higher recrystallization texture fraction. Enhanced recrystallization textures promote grain orientation randomization, reducing performance directionality from texture variations and optimizing overall mechanical properties [35–38].

4. Conclusions

This work investigated the effects of initial ingot thickness (400 mm vs. 520 mm) and rolling direction variations on the microstructures and mechanical properties of ultrahigh-strength Al-Zn-Mg-Cu alloy. Key findings are summarized as follows:

Significant directional variations in average grain size were observed. The 400-L route (400 mm ingot, 80% reduction) resulted in narrower coarse grain bands on the rolling plane compared to the 520-L and 520-LT routes, yet produced slightly wider bands on the rolling side plane. Both rolling and side planes revealed marginally larger grain sizes in the 520-L sample and 520-LT sample than that in the 400-L sample. The substantially greater thickness reduction in the 520-L and 520-LT sample processing significantly increased their GND density relative to 400-L.

Distinct textures emerged across processing routes. The 400-L processing route (400 mm ingot, 80% reduction) promoted a dominant S {123}<634> texture, whereas the Brass {011}<211> component prevailed in both the 520-L and 520-LT routes (520 mm ingot, 85% reduction). Shear texture components (E, Rotated Cube, F) were more prevalent in 400-L than in 520-L/520-LT. Recrystallization texture content progressively increased from 400-L to 520-L to 520-LT, with the latter showing the highest fraction, contributed by the greater cumulative strain and bidirectional rolling deformation.

The 400-L route exhibited pronounced anisotropy, with nearly identical yield strength and elongation in the L/LT directions (8.9% higher than the ST direction). Both the 520-L and 520-LT routes demonstrated enhanced ST-direction yield strength, effectively mitigat-

ing anisotropy. Notably, the 520-LT sample achieved a yield strength of 528 MPa in the ST direction, reducing the L-ST strength differential to just 5.8%.

Based on the findings of this study, for the production of 80 mm thick Al-Zn-Mg-Cu alloy plates, the following processing recommendations can be made. Where minimizing mechanical anisotropy and enhancing short-transverse (ST) properties are the primary objectives, the 520-LT processing route—i.e., a large initial ingot (520 mm) combined with cross-rolling (width spreading followed by longitudinal rolling)—is recommended. This deformation scheme promotes a transition in the dominant texture from the S {123}<634> component to the Brass {011}<211> component, thereby elevating the ST yield strength to 528 MPa and reducing the L–ST strength differential to less than 6%. This effectively mitigates the long-standing issue of ST strength deficits in thick plates. Conversely, when ST-direction performance is of secondary importance, the simpler unidirectional rolling route (520-L) offers a more cost-effective alternative.

Author Contributions: Methodology, G.D. and K.M.; Formal analysis, Y.W., X.Z. (Xu Zheng), X.Z. (Xinkui Zhang) and K.M.; Investigation, G.D. and Y.W.; Writing—original draft, G.D. and X.Z. (Xu Zheng); Writing—review & editing, G.D., X.Z. (Xu Zheng), X.Z. (Xinkui Zhang), K.M., B.X. and Z.M. All authors have read and agreed to the published version of the manuscript.

Funding: This work was supported by the Guangxi Key Research and Development Plan (AA23023031, AB23026138); Nanning City innovation and entrepreneurship leading talents "Yongjiang Plan" project (2022002); and China Association for Science and Technology Youth Talent Support Project (YESS20230008). The authors thank the Sinoma Institute of Materials Research (Guangzhou) Co., Ltd. (SIMR) for its support in TEM testing.

Informed Consent Statement: Not applicable.

Data Availability Statement: The original contributions presented in this study are included in the article. Further inquiries can be directed to the corresponding authors.

Conflicts of Interest: Authors Guiying Deng and Xu Zheng were employed by the company Guangxi Nannan Aluminum Processing Co., Ltd . The remaining authors declare that the research was conducted in the absence of any commercial or financial relationships that could be construed as a potential conflict of interest.

References

1. Chao, L.; He, Y.; Heng, L.; Nian, S.; Jin, F.; Lihua, Z. Dependence of creep age formability on initial temper of an Al-Zn-Mg-Cu alloy. *Chin. J. Aeronaut.* **2016**, *29*, 1445–1454.
2. Zheng, G.; Li, H.; Lei, C.; Fu, J.; Bian, T.; Yang, J. Natural aging behaviors and mechanisms of 7050 and 5A90 Al alloys: A comparative study. *Mater. Sci. Eng. A* **2018**, *718*, 157–164. [CrossRef]
3. Dursun, T.; Soutis, C. Recent developments in advanced aircraft aluminium alloys. *Mater. Des. (1980–2015)* **2014**, *56*, 862–871. [CrossRef]
4. Zwolak, M.; Śliwa, R. Analysis of the influence of dies geometry on the process extrusion force and properties of the extrudate obtained in the process of cold extrusion of 7075 aluminum alloy by the KOBO method. *Mater. Sci.-Pol.* **2024**, *42*, 92–106. [CrossRef]
5. Li, H.; Bai, Q.; Li, Y.; Du, Q.; Katgerman, L.; Zhang, J.; Zhuang, L. Mechanical properties and cold cracking evaluations of four 7×××series aluminum alloys using a newly developed index. *Mater. Sci. Eng. A* **2017**, *698*, 230–237. [CrossRef]
6. Kuo, C.-H.; Lin, Z.-Y. Optimizing the high-performance milling of thin aluminum alloy plates using the Taguchi method. *Metals* **2021**, *11*, 1526. [CrossRef]
7. Yashin, V.V.; Beglov, E.D.; Aryshensky, E.V.; Latushkin, I.A. Large size metal-clad ingots rolling process analysis using finite elements method. *J. Sib. Fed. Univ. Eng. Technol.* **2018**, *11*, 419–426.
8. Prabhu, T.R. An overview of high-performance aircraft structural Al alloy-AA7085. *Acta Metall. Sin. (Engl. Lett.)* **2015**, *28*, 909–921. [CrossRef]
9. Zhang, X.; Chen, Y.; Hu, J. Recent advances in the development of aerospace materials. *Prog. Aerosp. Sci.* **2018**, *97*, 22–34. [CrossRef]

10. Zare, M.A.; Taghiabadi, R.; Ghoncheh, M.H. Effect of cooling rate on microstructure and mechanical properties of AA5056 Al-Mg alloy. *Int. J. Met.* **2022**, *16*, 1533–1543. [CrossRef]
11. Dai, Y.; Yan, L.; Hao, J. Review on micro-alloying and preparation method of 7xxx series aluminum alloys: Progresses and prospects. *Materials* **2022**, *15*, 1216. [CrossRef] [PubMed]
12. Zhu, C.; Zhao, Z.; Zhu, Q.; Wang, G.; Zuo, Y.; Li, Q.; Qin, G. Hot-top direct chill casting assisted by a twin-cooling field: Improving the ingot quality of a large-size 2024 Al alloy. *J. Mater. Sci. Technol.* **2022**, *112*, 114–122. [CrossRef]
13. Li, Z.; Li, Y.; Zhou, R.; Xie, L.; Wang, Q.; Zhang, L.; Ji, Q.; Xu, B. Microstructure and properties of semi-solid 7075 aluminum alloy processed with an enclosed cooling slope channel. *Crystals* **2023**, *13*, 1102. [CrossRef]
14. Song, L.; Xie, Z.; Gao, H.; Kong, C.; Yu, H. Microstructure and mechanical properties of ARB-processed AA1050/AA5052 multilayer laminate sheets during cryorolling. *Mater. Lett.* **2022**, *307*, 130998. [CrossRef]
15. Roth, C.C.; Fras, T.; Mohr, D. Dynamic perforation of lightweight armor: Temperature-dependent plasticity and fracture of aluminum 7020-T6. *Mech. Mater.* **2020**, *149*, 103537. [CrossRef]
16. Chakraborty, P.; Singha, M.K.; Tiwari, V. Anisotropic mechanical response of AA7475-T7351 alloy at different loading rates and temperatures. *Thin-Walled Struct.* **2023**, *188*, 110842. [CrossRef]
17. Wei, L.; Pan, Q.; Huang, H.; Feng, L.; Wang, Y. Influence of grain structure and crystallographic orientation on fatigue crack propagation behavior of 7050 alloy thick plate. *Int. J. Fatigue* **2014**, *66*, 55–64. [CrossRef]
18. Yang, S.; Yang, Y.; Chen, Z. Effects of rolling method on the microstructure and anisotropy of mechanical properties of Cu–15Cr in-situ composites. *Mater. Sci. Eng. A* **2022**, *856*, 144000. [CrossRef]
19. Shin, Y.-C.; Park, Y.-C.; Hong, J.-P.; Cheong, J.Y.; Kim, K.-Y.; Shin, B.; Jeong, D.-Y.; Lee, T.; Kwak, T.; Jung, T.-K.; et al. Cross-rolling induced texture randomization and structural evolution for improved plastic isotropy in Al-Mg alloys with high Mg content. *J. Alloys Compd.* **2024**, *1008*, 176530. [CrossRef]
20. Pang, H.; Lu, L.; Yang, R.; Ma, M.; Wang, X.; Wu, Y.; Jing, L.; Dong, J.; Zhang, S. Investigation into Mg-4.5 Al-2.5 Zn Mg alloy applying cryogenic treatment and cross-rolling at diverse temperatures. *J. Mater. Res. Technol.* **2025**, *37*, 4064–4076. [CrossRef]
21. Ma, Z.; Zhong, T.; Sun, D.; Qian, B.; Turakhodjaev, N.; Betsofen, S.; Wu, R. Microstructure and anisotropy of mechanical properties of Al-3Li-1Cu-0.4 Mg-0.1 Er-0.1 Zr alloys prepared by normal rolling and cross-rolling. *Metals* **2023**, *13*, 1564. [CrossRef]
22. Kazemi-Navaee, A.; Jamaati, R.; Aval, H.J. Effect of single roll drive cross rolling on the microstructure, crystallographic texture, and mechanical behavior of Al-Zn-Mg-Cu alloy. *Arch. Civ. Mech. Eng.* **2022**, *22*, 41. [CrossRef]
23. Mondal, C.; Singh, A.K.; Mukhopadhyay, A.K.; Chattopadhyay, K. Effects of different modes of hot cross-rolling in 7010 aluminum alloy: Part I. Evolution of microstructure and texture. *Metall. Mater. Trans. A* **2013**, *44*, 2746–2763. [CrossRef]
24. Chen, Z.; Yan, K.; Ren, C.; Naseem, S. Precipitation sequence and hardening effect in 7A85 aluminum alloy. *J. Alloys Compd.* **2021**, *875*, 159950. [CrossRef]
25. Zhao, Y.; Liu, J.; Topping, T.D.; Lavernia, E.J. Precipitation and aging phenomena in an ultrafine grained Al-Zn alloy by severe plastic deformation. *J. Alloys Compd.* **2021**, *851*, 156931. [CrossRef]
26. Altuntaş, G.; Özdemir, A.T.; Bostan, B. Investigation of the impacts of artificial ageing, re-ageing and cryogenic cycles on multiplex second phase precipitation and life-time prediction in 7075 alloy. *Mater. Today Commun.* **2024**, *40*, 109602. [CrossRef]
27. Liu, E.; Pan, Q.; Liu, B.; Ye, J.; Wang, W. Microstructure Evolution of the Near-Surface Deformed Layer and Corrosion Behavior of Hot Rolled AA7050 Aluminum Alloy. *Materials* **2023**, *16*, 4632. [CrossRef] [PubMed]
28. Li, J.; Jiang, F.; Li, Y.; Zhang, M.; Chen, C.; Yang, Z.; Zhang, F. Effect of warm-rolling on the strength and ductility of multilayered composite steel. *Mater. Sci. Eng. A* **2022**, *841*, 143043. [CrossRef]
29. Kumar, D.S.; Chakradhar, I.; Rao, S.; Puri, R.; Manjini, S. Analysis of Chip Generation During Bar Rolling. *J. Fail. Anal. Prev.* **2018**, *18*, 635–639. [CrossRef]
30. Li, C.-M.; Cheng, N.-P.; Chen, Z.-Q.; Li, X.; Xie, Z.-J.; He, H. Electric field-induced aging phase transformation in Al-Zn-Mg-Cu alloys: A first-principles study. In Proceedings of the 2016 3rd International Conference on Mechatronics and Information Technology, Shenzhen, China, 9–10 April 2016; Atlantis Press: Dordrecht, The Netherlands, 2016; pp. 511–518.
31. Balaško, T.; Nagode, A.; Li, J.; Medved, J. Microstructure evolution during solution annealing of an Al–Zn–Mg–Cu alloy with La additions. *Sci. Rep.* **2025**, *15*, 3845. [CrossRef]
32. Wang, Z.; Huang, S.; Zhang, W.; Li, S.; Liu, J. Precipitation Thermodynamics in an Al–Zn–Mg Alloy with Different Grain Sizes. *Metals* **2024**, *14*, 625. [CrossRef]
33. Sun, J.-R.; Dong, B.-X.; Yang, H.-Y.; Shu, S.-L.; Qiu, F.; Jiang, Q.-C.; Zhang, L.-C. The Role of Lithium in the Aging Precipitation Process of Al-Zn-Mg-Cu Alloys and Its Effect on the Properties. *Materials* **2023**, *16*, 4750. [CrossRef] [PubMed]
34. Yan, X.; Yang, Y.; Hamada, H. Tensile properties of glass fiber reinforced polypropylene composite and its carbon fiber hybrid composite fabricated by direct fiber feeding injection molding process. *Polym. Compos.* **2017**, *39*, 3564–3574. [CrossRef]
35. Duan, X.; Jiang, H.; Mi, Z.; Cheng, L.; Wang, J. Reduce the Planar Anisotropy of AA6016 Aluminum Sheets by Texture and Microstructure Control. *Crystals* **2020**, *10*, 1027. [CrossRef]

36. Lee, D.N.; Han, H.N. Recrystallization textures of metals and alloys. In *Recent Developments in the Study of Recrystallization*; InTechOpen: London, UK, 2013; pp. 3–59.
37. Ryu, J.H.; Lee, D.N. The effect of precipitation on the evolution of recrystallization texture in AA8011 aluminum alloy sheet. *Mater. Sci. Eng. A* **2002**, *336*, 225–232. [CrossRef]
38. Inoue, H.; Takasugi, T. Texture control for improving deep drawability in rolled and annealed aluminum alloy sheets. *Mater. Trans.* **2007**, *48*, 2014–2022. [CrossRef]

Disclaimer/Publisher's Note: The statements, opinions and data contained in all publications are solely those of the individual author(s) and contributor(s) and not of MDPI and/or the editor(s). MDPI and/or the editor(s) disclaim responsibility for any injury to people or property resulting from any ideas, methods, instructions or products referred to in the content.